

## **Coring and Fragmentation of Elastomeric Needle Shield in a Pre-Filled Syringe**

Sahab Babae, Sean Teller, Kavin Kowsari, et al.

*PDA J Pharm Sci and Tech* **2025**, 79 274-284

Access the most recent version at doi:[10.5731/pdajpst.2024-003041.1](https://doi.org/10.5731/pdajpst.2024-003041.1)

## RESEARCH

# Coring and Fragmentation of Elastomeric Needle Shield in a Pre-Filled Syringe

SAHAB BABAEE<sup>1</sup>, SEAN TELLER<sup>2</sup>, KAVIN KOWSARI<sup>1</sup>, NIKOLAOS VASIOS<sup>2</sup>, STEVEN C. PERSAK<sup>1</sup>, NAGI ELABBASI<sup>2</sup>, and GUANGLI HU<sup>1,\*</sup>

<sup>1</sup>Device Development & Technology, Merck Research Laboratories, Merck & Co., Inc., Rahway, NJ 07065; and

<sup>2</sup>Veryst Engineering LLC, Needham, MA 02494 © PDA, Inc. 2025

**ABSTRACT:** Elastomeric components such as closures and stoppers play key roles in providing container closure integrity (CCI), supporting a portfolio of injectable combination products and primary containers including needle shields (NSs) in prefilled syringes (PFSs). Upon piercing through the elastomeric (i.e., synthetic rubber) components, the physical interaction between the needle and the deformable elastomer could result in the formation of small, random-shaped particles fragmented and dislodged from the NS material due to cutting processes. This phenomenon, called coring, poses a major risk in drug product contamination, as elastomer particle fragments can potentially be aspirated with the medication and injected into a patient or prevent injection. Here, we present a combined computational and experimental approach to assess the incidence of coring. In particular, we first experimentally characterized the nonlinear finite deformation behavior of five commonly used NS elastomers and calibrated constitutive models. Then, we performed finite element simulations validated with needle insertion experiments to compare the coring behavior of the NS elastomers. We demonstrated that higher maximum failure strain under tension and higher deformation-stiffening properties of the elastomer are contributing factors that attenuate coring and fragmentation. The experimental-numerical framework presented is suitable for quantifying broad correlative and discovering relationships between device properties governing the incidence of coring and fragmentation.

**KEYWORDS:** Prefilled syringe, Rigid needle shield, Coring, Elastomer material, Numerical modeling.

## Introduction

Needle coring has been a long-standing concern among clinicians. It is a phenomenon by which fragments of rubber are torn off as a needle penetrates the rubber stopper of a medication vial. The pieces of the rubber stopper sheared off by the bevel tip could be lodged in the bore of the draw needle, leading to clogging and drug contamination. In addition to vial stoppers, the material that cores the needle can be the elastomeric needle shield (NS) as a component of prefilled syringe (PFS) combination products or a patient's own tissue during injection. Elastomeric cores dislodged from the bulk NS material can be aspirated into a syringe and potentially injected into a patient (1), thereby coring

poses issues with both safety and patient experience (e.g., potential for deleterious physiological effects). Studies have reported incidences of coring varying between 3% and 97% (2, 3), and 40.8% when a blunt safety needle was used versus 4.2% using a sharp 18 G needle (1), with clinical implications ranging from undetectable granuloma formation, localized ischemia by inadvertent injection of a cored particle into an artery, and anaphylactic reactions to organ failure and death (4). As such, coring is a potential cause of morbidity and mortality and is likely underreported (5). On the other hand, the biological safety implication of small-particle rubber is still not fully understood (6, 7). Although none of the following techniques is failproof, common practices to attenuate coring have largely focused on manual inspection, altering the angle of entry into the rubber vial stopper or tissue (5), orienting the needle bevel upward, controlling the aspiration pressure, using small-gauge needles and changing the syringe size (8, 9), and utilizing PFSs. Others have elected to avoid the use of blunt drawing needles altogether (10) or adopted specialized syringe attachments

\* Corresponding Author: Device Development & Technology, Merck Research Laboratories, Merck & Co., Inc., Rahway, NJ 07065; E-mail: guangli.hu@merck.com  
doi: 10.5731/pdajpst.2024-003041.1

to decrease the incidence of coring (11), which has led to other complications related to those devices (12). Use of filter needles for loading medication into syringes may eliminate particulate fragments; however, filter implementation is not readily feasible in ready-to-inject PFS products. As discussed, these mitigation strategies have limited applications to PFSs, and these all neglect the root of the issue: material failure of the elastomeric NS. There is limited knowledge on how mechanical material properties influence coring performance, thus more detailed research is needed to document the true incidence of coring and test which strategies of medication aspiration or infusion are most effective to mitigate the risk of coring.

We developed an experimental-numerical framework that includes several model cases to gain fundamental insight into the physics of coring and potentially identify design pathways to prevent the associated clinically relevant risks. Given the inherently complex nature of the needle-NS interaction, we used finite element (FE) modeling to capture the important coring response of five elastomers directly obtained from commercial PFS products. To the authors' knowledge, predictive computational models characterizing needle coring have not yet been reported. It is noteworthy that coring is not a single aspect of rigid needle shield (RNS) material candidate selection. Complementary attributes of critical importance include biocompatibility and vapor/oxygen transmission rate through the elastomer, hence product-based evaluation must accompany material downselection.

## Materials and Methods

In the graphs below, we will provide a detailed overview of sample preparation for mechanical testing, the development of constitutive models for elastomeric materials, and the framework for numerical simulations.

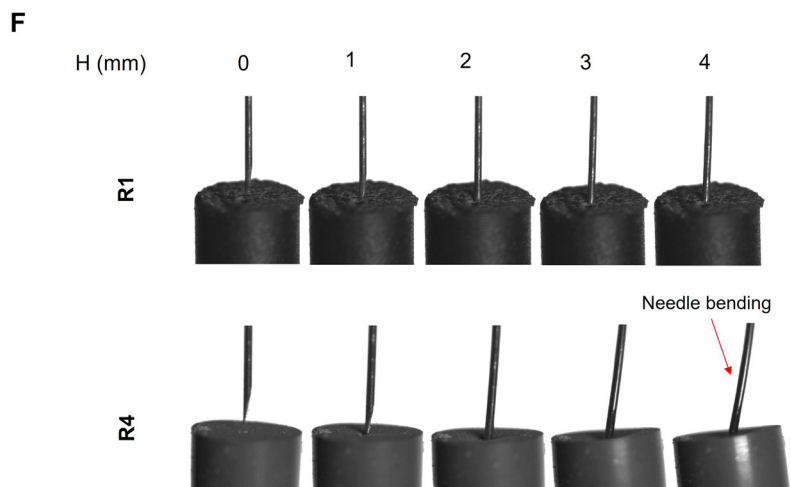
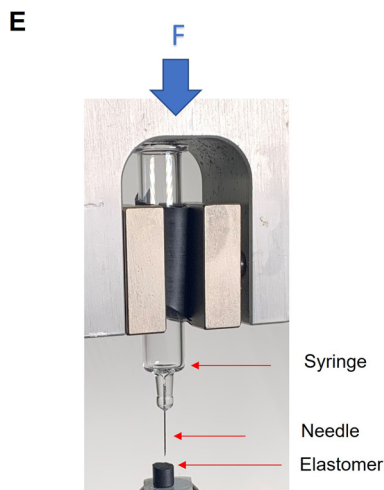
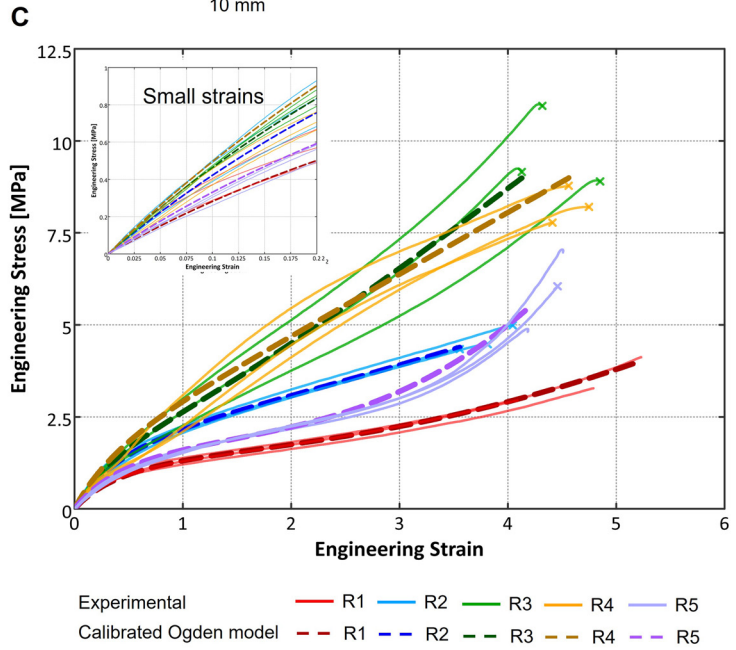
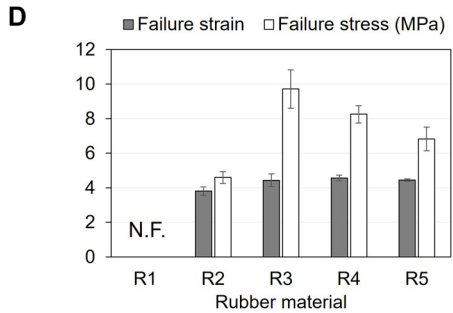
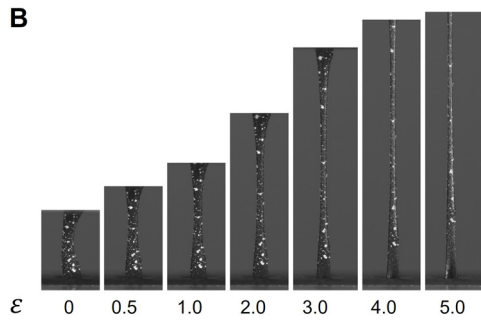
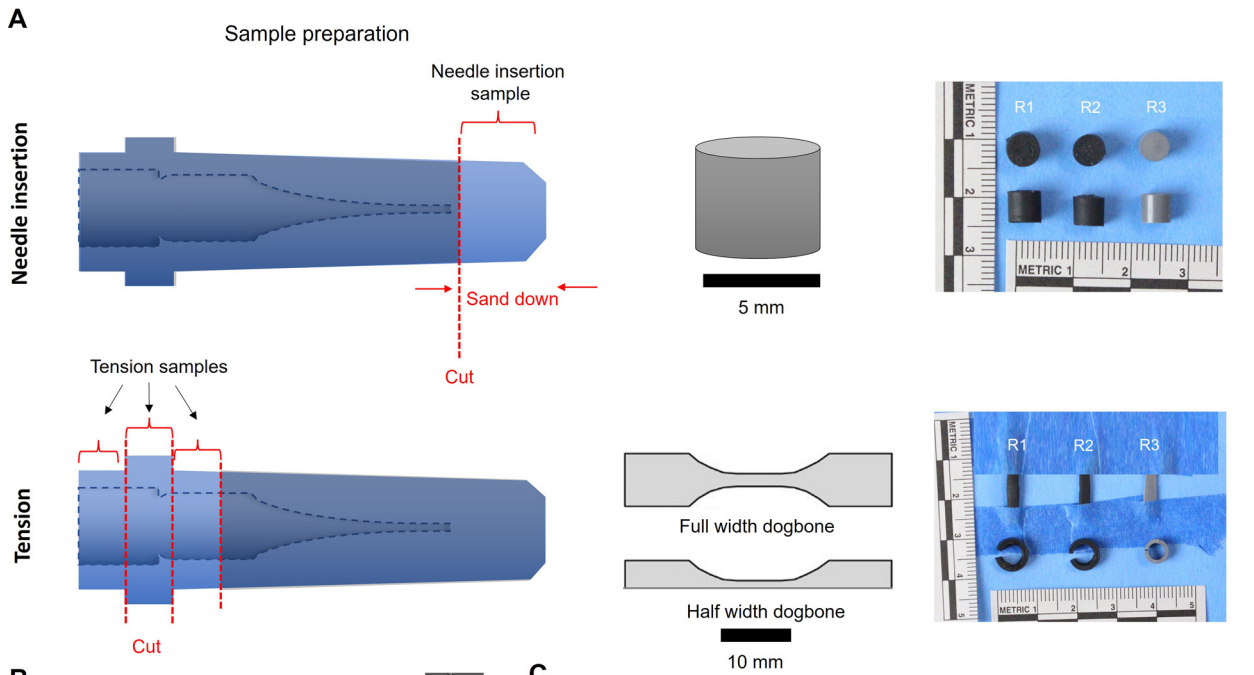
### *Materials, Sample Preparation, and Mechanical Tension Testing*

Five commercial elastomeric NS samples, labeled R1, R2, R3, R4, and R5, were selected for this study. Due to the small amount of material available in the RNS, we were not able to use standard sizes. We prepared experimental rubber samples by extracting strips of material directly from the five NS samples. Cylindrical blocks were extracted from forward sections for needle insertion tests (Figure 1A, top), while tensile strips were cut from the aft section of the RNS, flattened, and sculpted into full and half dog-bone geometries (Figure 1A, bottom). We determined that this

method gave us the most uniform test samples, with a rectangular cross section and repeatable test data. We used calipers to measure the width and thickness of the gage section at three points and computed the average area for these measurements. We applied a speckle pattern with a light coating of black and white paint for strain analysis using digital image correlation (DIC) and Correlated Solutions' Vic-2D software. We performed uniaxial tensile tests using full and half dog-bone samples with an electromechanical load frame and screw style tensile grips from AdMet at a displacement rate of 1 mm/s, with a nominal strain rate of 0.2/s. The tension tests were conducted using AS D638-14 as a guideline.

We used DIC (Figure 1B and Figure S-1) to measure engineering strain throughout the progressive deformation to characterize the stress-strain responses of R1-R5 samples as reported in Figure 1C. We calibrated a constitutive model (a third order hyperelastic Ogden model) for the rubber materials (dashed lines in Figure 1C, see "Constitutive Models of Elastomeric Needle Shields" in Methods and Table S-I for the material model calibration and coefficients). The calibrated models showed excellent agreement with the experimental curves over the entire strain range, particularly as the materials approach failure. The calibrated Ogden material models have a normalized mean absolute difference error (NMAD) of 3.6%, 2.9%, 0.10%, 9.7%, and 6.0% for R1, R2, R3, R4, and R5, respectively. The models with higher errors correspond to experimental data with more scatter, which is likely driven by sample preparation methods from the limited material available in the elastomeric NS. At small strains (inset of Figure 1C), the models match the results well, although R4 shows a higher stress response. We expect this to have a small impact on the results of the coring simulation, as a majority of the deformation is at higher stress and strains where the material model is more accurate.

Figure 1C shows that all the samples failed during tension testing before reaching out to engineering strain  $\epsilon = 5$ , except R1 that stretched over 500% without failure, indicating that R1 is more ductile than the other materials. R3 and R4 exhibited comparable engineering stress-strain behavior with larger stresses at failure (i.e., higher stiffness), whereas R2 and R5 underwent lower stresses during elongation (Figure 1D). We additionally performed notched tension tests to ensure all elastomers including R1 arrived at failure. DIC snapshots at zero strain and nonuniform strain fields before tears (i.e., propagated through each cross-section



leading to complete failure) as well as the corresponding stress–strain curves are provided in Figure S-2.

### Constitutive Models of Elastomeric Needle Shields

The constitutive behavior of the rubber candidates was captured using a third order hyperelastic Ogden material model (15), whose strain energy function is  $U = \sum_{i=1}^3 2\mu_i (\bar{\lambda}_1^{\alpha_i} + \bar{\lambda}_2^{\alpha_i} + \bar{\lambda}_3^{\alpha_i} - 3)/\alpha_i^2 + \sum_{i=1}^3 (J - 1)^{2i}/D_i$ , where  $\mu_i$ ,  $\alpha_i$ ,  $D_i$ ,  $i = 1, 2, 3$  are the model parameters reported in Table S-I. Here,  $\bar{\lambda}_i = J^{-1/3}\lambda_i$ ,  $i = 1, 2, 3$  represent the deviatoric principal stretches,  $\lambda_i$ ,  $i = 1, 2, 3$  are the principal stretches,  $J = \det(\mathbf{F})$ , and  $\mathbf{F}$  is the deformation gradient. Four of the Ogden model parameters are related to the conventional initial shear modulus, denoted by  $G_0$ , and initial bulk modulus, denoted by  $K_0$ , at zero strain:  $G_0 = \mu_1 + \mu_2 + \mu_3$ ,  $K_0 = 2/D_1$ . Material failure is not explicitly captured in the Ogden model.

### Needle Insertion Tests

We started experimental characterization of the coring behavior using perpendicular needle insertion tests. We performed the needle insertion tests by displacing the needle 4 mm down into the cylindrical samples. We cut cylindrical samples for needle insertion tests from the RNS using a scalpel, with the cut lines shown in Figure 1A. After cutting, we ground the ends to make a more uniform surface on the needle insertion side and to remove the chamfers on the as-manufactured end. We performed needle insertion tests using staked-in standard 25 G needles to cut into cylindrical specimens, which were secured using a double-sided

tape, at an insertion rate of 1 mm/s to a depth of 4 mm. We aligned the needle to be perpendicular and centered on the cylindrical specimen and inserted the needle with an AdMet universal test frame, measuring force and displacement as well as recording the test with a digital video camera. We inspected the needle visually after each test to determine if the needle was clogged and did not notice any clogged needles. Each material was tested  $n = 3$  times.

The experimental setup used to cut into the prepared cylindrical R1–R5 specimens is shown in Figure 1E (see “Needle Insertion Test” in Methods, and Video S-1 illustrating the insertions of standard 25 G needles into all five elastomer blocks and the corresponding force–displacement curves). The snapshots of needle insertion into R1 (low stiffness) and R4 (high stiffness) cylindrical rubber specimens at different levels of applied displacement,  $H = 0, 1, 2, 3$ , and 4 mm, are presented in Figure 1F. Negligible tilting of the rubber with a small needle deflection was recorded during the needle insertion into R1. However, the stainless-steel needle experienced a substantial degree of visible bending, despite its high elastic modulus, as it entered R4. The excessive tilting of R4 caused small deviations in the insertion angle, which were less evident in the lower-stiffness elastomer, R1, although they did not significantly impact the force response.

### Numerical Simulations

All the simulations were carried out using the commercial FE package Abaqus 2020 (SIMULIA, Providence, RI). We determined the Coupled Eulerian Lagrangian

## Figure 1

**Experimental characterization of the elastomeric needle shields and needle insertion tests. (A) Sample preparation for needle insertion (cylindrical specimens, top) and uniaxial tension (dog-bone and half dog-bone specimens, bottom) tests. Three exemplary rubber samples R1, R2, and R3 are shown. (B) Exemplary digital image correlation (DIC) snapshots showing the progressively deformed shape of the half dog-bone sample R1 under uniaxial tensile loads at different levels of applied engineering strain,  $\varepsilon = 0, 0.5, 1.0, 2.0, 3.0, 4.0$ , and  $5.0$ . (C) Experimental engineering stress–strain response curves of R1–R5 under monotonic uniaxial tension tests (solid lines) tested at 1 mm/s. The dashed lines are calibrated hyperelastic Ogden material models. The inset shows the small-strain behavior. The x marker represents failure. (D) Engineering failure strains and stresses of the five rubber candidates under uniaxial tensile tests up to  $\varepsilon = 5$ . The data is reported as mean  $\pm$  S.D. of  $N = 3$  measurements for each group. NF denotes no failure observed. (E) Experimental setup used for needle insertion testing. (F) Experimental snapshots showing needle insertion into R1 (negligible tilt with a small needle deflection) and R4 (excessive tilt with a large needle deflection) cylindrical rubber specimens at different levels of applied displacement,  $H = 0, 1, 2, 3$ , and 4 mm.**

(CEL) technique as the most viable candidate for the needle insertion problem, as it is able to support the necessary material model definition, large deformations, and sharp boundaries (i.e., needle geometry) and can handle cutting of materials well. In contrast to implicit Lagrangian methods, the explicit CEL method can be more computationally expensive but handles contact, cutting, and material failure without an explicit failure model and is explicitly stable. The fully Lagrangian Abaqus Explicit approach requires a detailed definition of the material failure conditions and is error-prone or fails for some material model–needle combinations (i.e., not a reliable choice for this problem), and due to the element sizes needed for a Lagrangian method, the fully Lagrangian approach is slower than the CEL. We generated three-dimensional (3D) FE models of the needle (imported from SolidWorks) and the five rubber candidates to simulate the needle insertion process and investigate RNS coring.

We modeled the 25 G standard needle (inner diameter of 0.277 mm and outer diameter of 0.385 mm) as a rigid body with no strain using a rigid body constraint and the rubber samples as nonlinear hyperelastic elastomers described in “Constitutive Models of Elastomeric Needle Shields”. Two element types were used to construct the model: tetrahedral quadratic modified element (Abaqus element type C3D10M, seed size = 50  $\mu\text{m}$ ) for the needle and linear quadrilateral element (Abaqus element type EC3D8R, seed size = varied from 35  $\mu\text{m}$  to 90  $\mu\text{m}$ , with smaller elements near the needle insertion) for the elastomers. We applied a constant displacement rate of 1 mm/s. We used a rigid body coupling for the needle to simulate the body as a rigid body. We performed a mesh refinement study and verified that the FE solutions are convergent results and are not severely affected by small changes in mesh size. We simulated the problem in a 3D computational domain and used one symmetry plane to fully define the geometry. We modeled the elastomer with a Eulerian domain that was sufficiently large to contain the material at the completion of the test, and the needle as a rigid Lagrangian representation. A significant part of the needle insertion force is likely due to friction between the outer circumference of the needle and the elastomer as well as a function of local surface topography that is not captured by the smooth surfaces in the numerical domain. As such, we simulated friction coefficients between 0.01, 0.1, 0.15, and 0.3, treated as a calibration parameter *in silico*, and improved model predictions to match experimental force-

displacement profiles. In particular, the friction coefficient corresponded to the sudden drops in the force vs. displacement curves. The authors chose the friction coefficients that best matched the tested response.

## Results and Discussion

Figure 2A illustrates a commercial PFS product with a two-component NS closure system, including a rigid thermoplastic cap encompassing the soft elastomer insert. The variation in sizes and geometries of the NS closure systems used in this study are presented in Figure S-3. Our hypothesis is that coring occurs in PFSs due to physical NS-needle interactions (i.e., cutting the elastomer and generating dislodged particles). We performed benchtop tests in which we inserted the PFS needle into the elastomeric NS. The contents of PFS injectate samples expelled and collected into separate beakers revealed visibly entrained submillimeter elastomeric particles with various shapes and sizes. Figure 2B shows an X-ray computed tomography scan of the representative damage to the elastomeric NS, as well as images showing the shapes and sizes from an optical microscope. Formation of cores (i.e., fragmented microparticles) not visible to the naked eye have been previously reported (4, 13, 14). The microparticles we found due to NS coring are consistent with the literature.

We aimed to develop predictive computational models characterizing needle coring. We constructed 3D numerical models of the 25 G needle and the five rubber materials (Figure 3A) and employed FE analyses to model the needle insertion problem and capture the large deformation of the rubber and potential coring. We used a CEL formulation with explicit time integration in the commercial FE package Abaqus (see “Numerical Simulations” in Methods). Figure 3B illustrates cross-sectional numerical snapshots showing progressively deforming elastomers at various applied displacement,  $H = 0, 1, 2, 3, 3.5,$  and  $4$  mm, throughout needle penetration into R1. The peninsula-shaped rubber fragments initially dislocate as the heel of the needle contacts R1, and full detachment from the bulk occurs at deeper penetrations. Such fragments will leave the needle upon injection and show up as coring particles. The insertion of the 25 G standard needle into R1–R5 rubber candidates obtained from FE simulations are presented in Video S-2.

The corresponding measured force-displacement profiles (solid lines) are reported in Figure 3C. The responses are

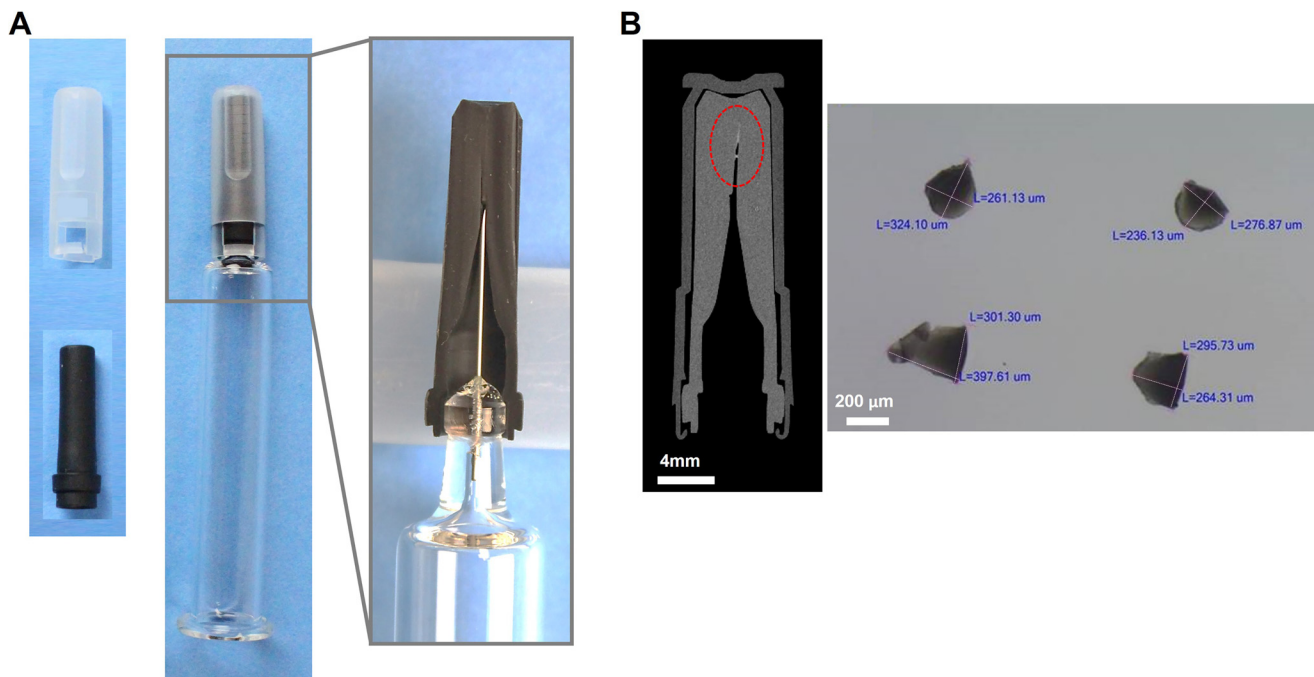


**Figure 2**

**Needle shield (NS) coring in a prefilled syringe (PFS).** (A) A PFS with a NS closure system (middle) composed of a rigid translucent thermoplastic cap and compliant rubber insert (left). Magnified cross-sectional view of the elastomeric NS in contact with the staked-in needle (right). (B) Representative X-ray computed tomography (XRCT) image of a NS after removal from a PFS. Visible elastomeric submillimeter particles detached from the rubber insert were observed suspended in the injectate after injecting the PFS.

characterized by a gradual linear increase with two force-drop occurrences at offsets of approximately 1.0 and 2.3 mm measured from the elastomeric cylinder's top surface (see Videos S-1 and S-2 for individual force-displacement curves). Inspection of the needle insertion tests and simulations revealed that these force-drops correspond to the instances as the tip and heel of the needle puncture the material, respectively. The drop in force value correlates with the release of elastic strain energy at the site of puncture, which was also reflected in the stress contours showing maximum von Mises stresses at the needle tip and heel (Figure 3B).

The simulations reproduced experimental force-displacement and elastomer separation leading to debris filling the needle core. Figure 3C superposes experimental-numerical force-displacement curves, revealing close agreement between the force magnitude vs displacement trend for R1–R5. CEL models have inherent limitations in constitutive models, which make advanced failure criteria difficult to implement. In our simulations and test results, we did not observe complete blockage of the needle core. The assumption of a

rigid needle can explain some of the discrepancy between the simulation and test results. In some tests (as shown in Figure 1F), the needle bends, changing the angle of insertion into the elastomeric NS. This can cause some discrepancies, but modeling the needle as deformable was computationally not tractable.

Based on the numerical simulations and experimental observations, the larger an elastomer's tensile failure strain and strain stiffening response, the more resistant the material is to the coring phenomenon. Using the failure strain and the strain-stiffening as favorable properties, R1–R5 are ranked as follows from the least to the most likely to experience coring during needle insertion: R1, R3, R4, R5, and R2. R1 having the largest failure strain among R1–R5 is expected to perform the best, whereas R2 with the lowest failure strain would exhibit the worst coring performance. R3 and R4 deliver similar coring performance, but R3 is expected to perform better as it features a higher strain stiffening at large strains. R5 has a lower failure strain than R1–R3 but is expected to perform better than R2 due to its substantial strain stiffening response at high strains.

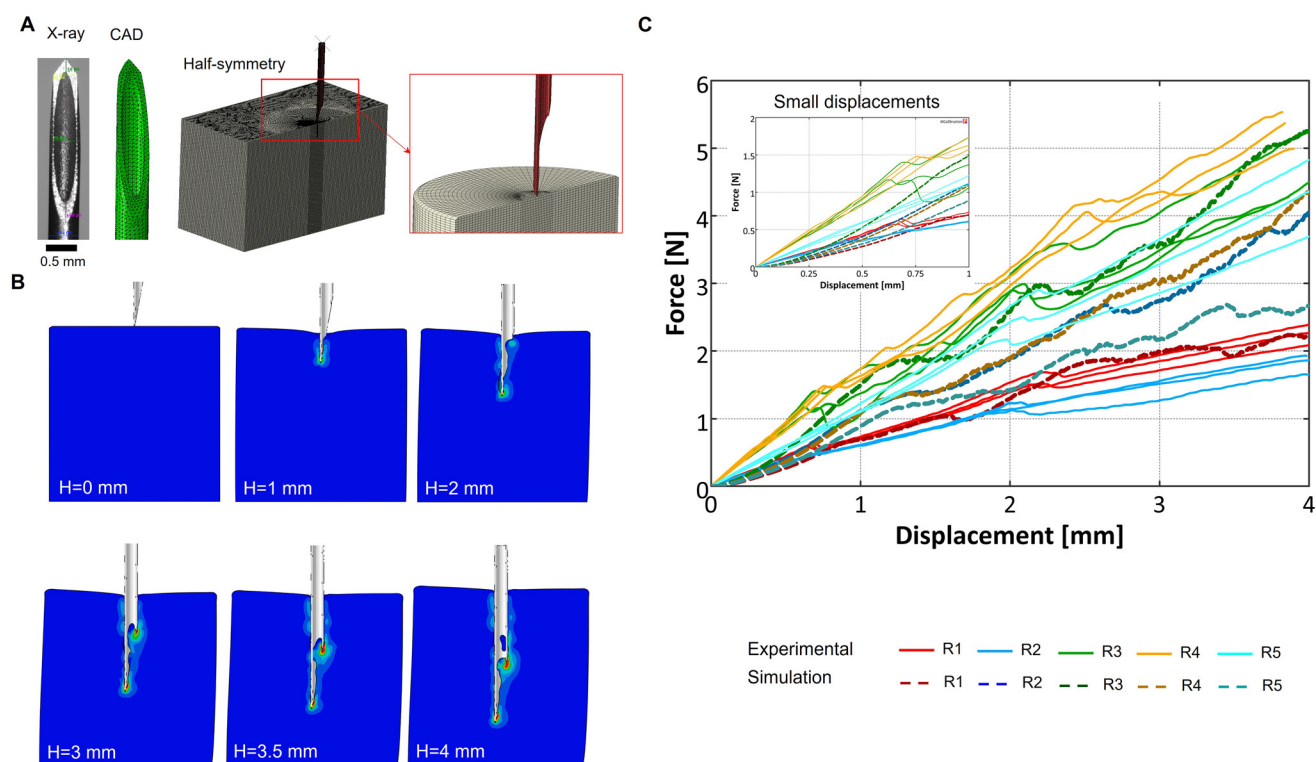


**Figure 3**

**Numerical characterization of needle insertion into the elastomeric needle shields. (A)** FE meshed model consists of a rigid 25 G needle based on the needle image and rubber matrix. **(B)** Representative numerical snapshots showing cross-sectional views of progressively deformed shapes of R1 at an insertion rate of 1 mm/s at various levels of applied displacement,  $H = 0, 1, 2, 3, 3.5,$  and 4 mm. **(C)** Experimental (solid lines) and numerical (dashed lines) needle insertion force as a function of insertion depth for R1–R5 samples at a constant uniaxial displacement rate of 1 mm/s. The inset shows small displacement behavior. The experimental data are reported for  $N = 3$  measurements for each group.

### Conclusion

Coring presents a risk of compromising patient safety and promoting drug contamination. To address this, the current study prospectively evaluated elastomeric RNS materials by developing an experimental-numerical workflow to bring insight into needle coring performance. We experimentally characterized five commercially available elastomeric materials and used this empirical data to calibrate finite-strain constitutive models. The FE simulations were validated by conducting needle insertion experiments. Based on our simulations and experimental observations, we determined that material properties of the elastomeric NS can significantly influence the incidence of coring. In particular, larger maximum strain-to-failure and stiffening with deformation suppressed coring. This study brings awareness about the potential implications of established numerical models, enabling the user to modify important parameters and investigate their

effects on coring, serving as a predictive tool to study the needle insertion problem. These FE simulations can predict the response of different material combinations, effect of needle geometry, influence of process conditions such as needle geometry, insertion rate, and orientation, on the resulting force-displacement responses and degree of coring. In particular, early *in silico* predictions of the needle and NS system can prevent failures later in the design process that prevent the timely release of a PFS system. Predicting needle coring early in the design process means that changes to the assembly process, manufacturing tolerances, materials, or needle designs are tractable. More comprehensive follow-up investigations to understand the impact of such potential underlying mechanisms are warranted. Additional work to use these predictive FE models to simulate different anticoring technology should be performed, including blunt vs. sharp needles, insertion angles, and needle designs. The current model framework has great potential to assist pharmaceutical companies in the informed selection and design of PFSs for novel therapies. By addressing this critical yet

often overlooked aspect during the early stages of combination product development, our approach can contribute to more effective and patient centric drug delivery solutions.

### Declaration of Interests

G. H., K. K., S. C. P., and S. B. are employees of Merck Sharp & Dohme LLC, a subsidiary of Merck & Co., Inc., Rahway, NJ, USA, and stockholders of Merck & Co., Inc., Rahway, NJ, USA. S.T., N.E., and N.V. are employees of Veryst Engineering LLC and declare that they have no known competing financial interests or personal relationships that could have appeared to influence the work reported in this paper.

### Acknowledgments

The authors would like to thank Wail Rasheed, Prakash Sundaramurthi, and Leon Farber of Merck & Co., Inc. for the technical discussion throughout this effort. Additionally, the authors would like to thank Jörgen Bergström (formerly at Veryst Engineering, LLC) for his early-stage technical insight into the problem.

### Funding Statement

This work is supported by Merck Sharp & Dohme LLC, a subsidiary of Merck & Co., Inc., Rahway, NJ, USA.

### Supplementary Materials

Experimental images of the PFS closure systems, mechanical characterization of the rubber materials, and videos of experimental/numerical force-displacement characterization of needle insertion into the elastomeric needle shields can be found in Supplementary Materials.

### References

1. Wani, T.; Wadhwa, A.; Tobias, J. D. The Incidence of Coring with Blunt versus Sharp Needles. *J. Clin. Anesth.* **2014**, *26* (2), 152–154.
2. Eskander, J.; Cotte, J.; Glenn, E.; Friedman, S.; Rosinia, F. The Incidence of Coring and Fragmentation of Medication Vial Rubber Stoppers. *J. Clin. Anesth.* **2015**, *27* (5), 442–444.
3. Kordi, R.; White, B. F.; Kennedy, D. J. Possibility and Risk of Medication Vial Coring in Interventional Spine Procedures. *PM&R* **2017**, *9* (3), 289–293.
4. Lehr, H.-A.; Brunner, J.; Rangoonwala, R.; Kirkpatrick, C. J. Particulate Matter Contamination of Intravenous Antibiotics Aggravates Loss of Functional Capillary Density in Postischemic Striated Muscle. *Am. J. Respir. Crit. Care Med.* **2002**, *165* (4), 514–520.
5. Hruska, J. L.; Saasouh, W.; Alhamda, M. S. Coring Revisited: A Case Report and Literature Review. *Cureus* **2022**, *14* (9), e29750.
6. Kirkpatrick, C. J.; Lehr, H. A.; Otto, M.; Bittinger, F.; Rangoonwala, R. Clinical Implications of Circulating Particulate Contamination of Parenteral Injections: A Review. *Crit. Care Shock* **1999**, *4*, 166–173.
7. Nyabadza, M. Preventing Latex Sensitisation and Foreign Body Micro-Emboli. *Anaesthesia* **2001**, *56* (7), 690–713.
8. Gragasin, F. S.; van den Heever, Z. A. The Incidence of Propofol Vial Coring with Blunt Needle Use is Reduced with Angled Puncture Compared with Perpendicular Puncture. *Anesth. Analg.* **2015**, *120* (4), 954–955.
9. Plumer, A. L. Principles and Practice of Intravenous Therapy. *AJN, Am. J. Nurs.* **1976**, *76* (1), 85.
10. Riess, M. L.; Strong, T. Near-Embolization of a Rubber Core from a Propofol Vial. *Anesth. Analg.* **2008**, *106* (3), 1020–1021.
11. Riess, M. L. A Recommended Solution for Avoiding Coring of a Rubber Stopper. *Anesth. Analg.* **2008**, *107* (3), 1084–1085.
12. Kohli, N.; Florence, F. B. Potentially Dangerous Fracture of the Needleless Interlink Vial Access Cannula. *Anesthesiology* **2005**, *102* (3), 703–704.
13. Asakura, T.; Seino, H.; Nozaki, S.; Abe, R. Occurrence of Coring in Insulin Vials and Possibility of Rubber Piece Contamination by Self-Injection. *Yakugaku Zasshi* **2001**, *121* (6), 459–463.
14. Sakai, O.; Furuse, M.; Nakashima, N. Cut-off Fragments of Rubber Caps of Bottles of Contrast Material: foreign Bodies in the Drip Infusion System. *AJNR Am. J. Neuroradiol.* **1996**, *17* (6), 1194–1195.
15. *Abaqus User's Manual*. Dassault Systèmes: Johnston, RI, 2020.

## Supplementary Materials

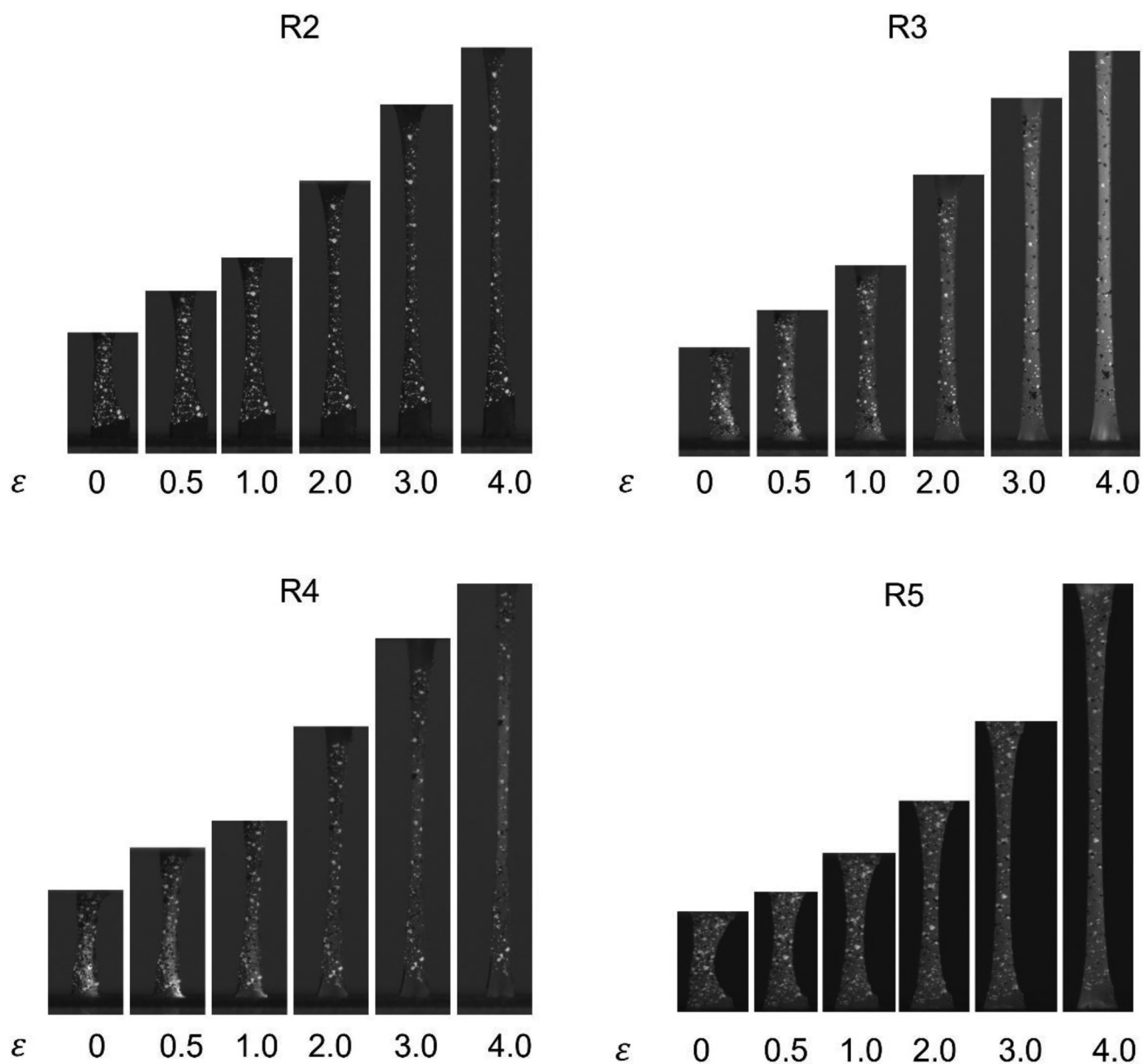


Figure S-1

Images of the rubber materials under monotonic tensile testing. The snapshots show the progressively deformed shape of R1, R2, R3, and R4 half dog-bone samples at different levels of applied engineering strain,  $\epsilon = 0, 0.5, 1.0, 2.0, 3.0,$  and  $4.0$ .

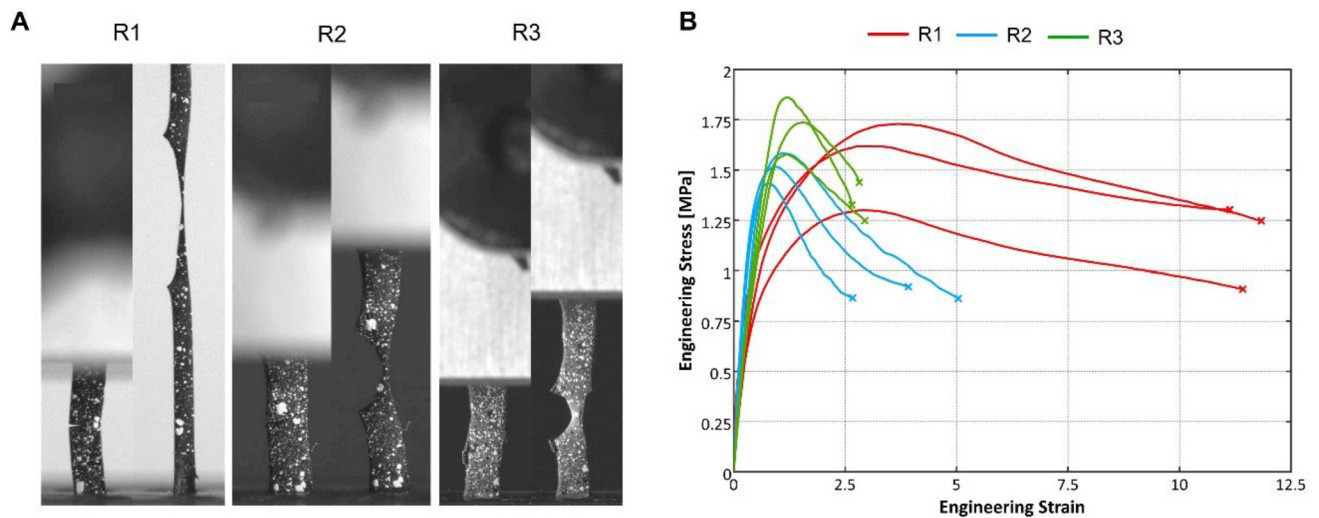


Figure S-2

Mechanical characterization of the notched elastomeric samples under notched tension. (A) Representative experimental digital image correlation (DIC) snapshots showing undeformed (left) and stretched configurations just before failure (right) for R1–R3 notched half dog-bone samples under tensile loads. A notch (approximately half the initial width of the samples) was cut into the test samples using a scalpel. These photos demonstrate that R1 is significantly more ductile than the other materials. (B) Experimental engineering stress–strain response under monotonic notched tension tests are shown (N=3 repeats). The x marker represents failure. The tests were performed with a constant displacement rate of 1 mm/s.

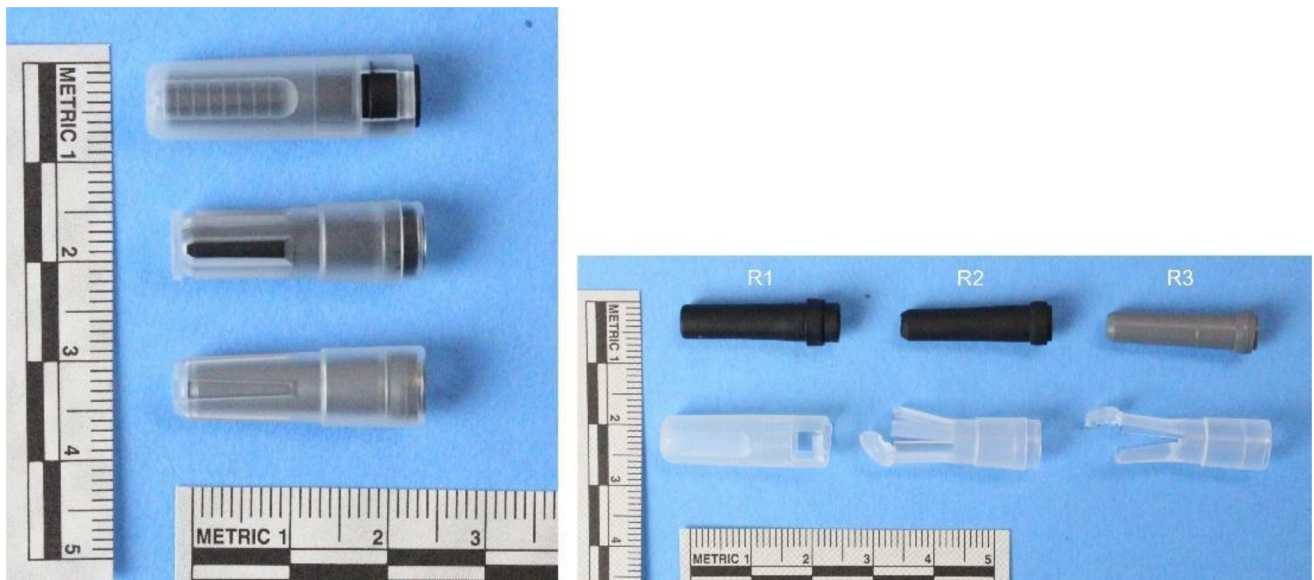


Figure S-3

Experimental images of the prefilled syringe (PFS) closure systems considered in the study. Three exemplary needle shield (NS) closure systems composed of translucent thermoplastic caps and elastomer inserts, R1, R2, and R3, are shown.

**TABLE S-I**  
**Model Parameters of the Third Order Constitutive Hyperelastic Ogden Material Models for the Five Rubber Candidates R1–R5.**

Parameter	R1	R2	R3	R4	R5	Units
$\mu_1$	0.726	0.562	-0.719	0.051	0.0100	MPa
$\mu_2$	0.291	0.322	1.27	1.14	1.22	MPa
$\mu_3$	0.0549	0.706	1.21	0.203	0.0154	MPa
$\alpha_1$	0.309	0.641	1.47	0.00933	5.24	None
$\alpha_2$	0.576	2.63	2.45	2.30	0.843	None
$\alpha_3$	3.53	0.479	-0.868	0.00114	0.812	None
$D_1$	0.02	0.02	0.02	0.02	0.02	1/MPa
$D_2$	0	0	0	0	0	1/MPa
$D_3$	0	0	0	0	0	1/MPa

#### Supplementary Videos

Supplementary videos S1 and S2 are available online.

# PDA Journal of Pharmaceutical Science and Technology



**An Authorized User of the electronic PDA Journal of Pharmaceutical Science and Technology (the PDA Journal) is a PDA Member in good standing. Authorized Users are permitted to do the following:**

- Search and view the content of the PDA Journal
- Download a single article for the individual use of an Authorized User
- Assemble and distribute links that point to the PDA Journal
- Print individual articles from the PDA Journal for the individual use of an Authorized User
- Make a reasonable number of photocopies of a printed article for the individual use of an Authorized User or for the use by or distribution to other Authorized Users

**Authorized Users are not permitted to do the following:**

- Except as mentioned above, allow anyone other than an Authorized User to use or access the PDA Journal
- Display or otherwise make any information from the PDA Journal available to anyone other than an Authorized User
- Post articles from the PDA Journal on Web sites, either available on the Internet or an Intranet, or in any form of online publications
- Transmit electronically, via e-mail or any other file transfer protocols, any portion of the PDA Journal
- Create a searchable archive of any portion of the PDA Journal
- Use robots or intelligent agents to access, search and/or systematically download any portion of the PDA Journal
- Sell, re-sell, rent, lease, license, sublicense, assign or otherwise transfer the use of the PDA Journal or its content
- Use or copy the PDA Journal for document delivery, fee-for-service use, or bulk reproduction or distribution of materials in any form, or any substantially similar commercial purpose
- Alter, modify, repackage or adapt any portion of the PDA Journal
- Make any edits or derivative works with respect to any portion of the PDA Journal including any text or graphics
- Delete or remove in any form or format, including on a printed article or photocopy, any copyright information or notice contained in the PDA Journal